

## On differences and similarities between static and continuous ultrasonic welding of thermoplastic composites

Jongbloed, B.C.P.; Teuwen, Julie J.E.; Benedictus, R.; Fernandez Villegas, I.

**DOI**

[10.1016/j.compositesb.2020.108466](https://doi.org/10.1016/j.compositesb.2020.108466)

**Publication date**

2020

**Document Version**

Final published version

**Published in**

Composites Part B: Engineering

**Citation (APA)**

Jongbloed, B. C. P., Teuwen, J. J. E., Benedictus, R., & Fernandez Villegas, I. (2020). On differences and similarities between static and continuous ultrasonic welding of thermoplastic composites. *Composites Part B: Engineering*, 203, Article 108466. <https://doi.org/10.1016/j.compositesb.2020.108466>

**Important note**

To cite this publication, please use the final published version (if applicable).  
Please check the document version above.

**Copyright**

Other than for strictly personal use, it is not permitted to download, forward or distribute the text or part of it, without the consent of the author(s) and/or copyright holder(s), unless the work is under an open content license such as Creative Commons.

**Takedown policy**

Please contact us and provide details if you believe this document breaches copyrights.  
We will remove access to the work immediately and investigate your claim.



# On differences and similarities between static and continuous ultrasonic welding of thermoplastic composites

Bram Jongbloed<sup>\*</sup>, Julie Teuwen, Rinze Benedictus, Irene Fernandez Villegas

Department of Aerospace Structures and Materials, Faculty of Aerospace Engineering, Delft University of Technology, Kluyverweg 1, 2629 HS Delft, The Netherlands

## ARTICLE INFO

### Keywords:

Fusion bonding  
Polymer mesh  
Continuous welded seam  
High frequency welding  
Joining

## ABSTRACT

Continuous ultrasonic welding is a promising high-speed and energy-efficient joining method for thermoplastic composite structures. Our aim was to identify and understand differences between the static and continuous ultrasonic welding process for thermoplastic composites. In particular, melting of the interface, consumed power and energy density, temperature evolution at the weld interface, and optimum welding conditions for both types of processes were investigated. This was done for three combinations of welding force and vibrational amplitude, parameters which are known to have a significant effect in both welding processes. Our results showed that for the continuous process the amount of non-welded area under the sonotrode remains constant, while for the static process the amount of non-welded area gradually decreases to zero. Additionally, the optimum vibration times and welding speeds in both processes are similar.

## 1. Introduction

Aircraft manufacturers are constantly aiming to reduce manufacturing and operational cost. Therefore, aircraft manufacturers are increasing their interest in fibre-reinforced polymer matrix composites. They allow tailoring of the mechanical properties, and they can have a higher specific strength and stiffness compared to metals. This makes it possible to reduce the weight of the aircraft structure. The lower structural weight typically reduces the operational cost of aircraft by for example a lower fuel consumption.

The matrix of the composites consists of either a thermoplastic or a thermosetting polymer. Especially fibre-reinforced polymer matrix composites with a thermoplastic matrix system can significantly reduce cost during part manufacturing and assembly as compared to fibre-reinforced thermosetting composites. The main contributing factors are the ease of manufacturing (e.g. hot press forming), the reduction in the cycle time, the high material toughness, the recyclability of entire components and scraps produced during manufacturing, and the possibility to weld the thermoplastic composite components together.

The use of resistance welding to assemble the fixed leading edge of the A380 [1], and the use of induction welding to assemble the rudder and elevators of the Gulfstream G650 [2], demonstrate the applicability of welding techniques in the aerospace industry. Another promising welding technique is ultrasonic welding. This technique is fast, energy efficient, and can potentially be monitored and controlled in situ. Especially with the expectation that for next generation aircraft

large structural components will be made from carbon fibre-reinforced thermoplastic composites, the need for a high-speed, and low-cost welding technique increases.

During the ultrasonic welding process, a sonotrode exerts high frequency, low amplitude vibrations to the to be welded parts, while, at the same time, applying a static force. These vibrations heat up the interface through frictional and viscoelastic heating [3,4]. Zhang et al. showed that the heating of the interface is initiated by surface friction, after the glass transition temperature of the thermoplastic material has been reached at the interface, the main heating mechanism becomes viscoelastic heating [4]. To focus heat generation at the interface a relatively thin resin-rich layer, called energy director is used [5,6]. The relatively low-stiffness energy director experiences a higher cyclic strain due to the vibrations and therefore heats up faster than the stiff adherends.

Most research in the field of ultrasonic welding of thermoplastic composites so far has focused on static welding of simple single lap shear samples [5–15]. Villegas et al. showed that during the static welding process different stages can be identified corresponding to heating up and melting of the interface [8]. Feedback data from the welder, more specifically power and vertical sonotrode displacement, could be used to identify these stages and in situ monitor and control the welding process [5,7]. Villegas et al. showed that by identifying stages in the welding process, it is possible to find combinations of parameters that consistently result in high strength joints [5,7].

<sup>\*</sup> Corresponding author.

E-mail address: [b.c.p.jongbloed@tudelft.nl](mailto:b.c.p.jongbloed@tudelft.nl) (B. Jongbloed).

Recently, continuous ultrasonic welding has shown to be a promising high-speed welding technique for carbon fibre-reinforced polyphenylene sulphide (CF/PPS) thermoplastic composites. For the continuous welding process the sonotrode moves over the to be welded overlap, while it applies the mechanical vibrations and static welding force [16]. Senders et al. demonstrated the possibility of welding two composite adherends together by using zero-flow welding with a 80 microns-thick flat energy director, i.e. a flat resin film, at the interface to focus the heat generation [16]. As a step forward, we continued to use the same composite material and experimental set-up and showed that the weld uniformity and quality could be improved by using a woven polymer mesh as energy director [17]. Additionally, continuous ultrasonic welding has been demonstrated as an efficient technique for tacking and, potentially, consolidating thermoplastic composite tapes during automated fibre placement (AFP) [18,19] and filament winding (FW) [20,21] processes. Such processes are however relatively different to the welding process subject of the present paper, since they deal with flexible pre-impregnated or semi-impregnated tapes instead of stiff composite adherends or parts.

In contrast to the static ultrasonic welding process of thermoplastic composite parts, the phenomena happening at the interface during the continuous ultrasonic welding process are not fully understood yet. As a result, the process of, for instance, finding an optimum welding speed (i.e. a speed that results in welded joints with the highest strength), is based on labour- and material-intensive trial-and-error procedures [16]. Contrarily, finding of optimum vibration times in static ultrasonic welding can be efficiently defined with the aid of in situ monitoring of the welding process [5]. Current understanding of the static ultrasonic welding process has been attained by studying a number of aspects of the process, among others:

- the melting phenomena of the interface. Fractography and cross-sectional microscopy were used by Villegas et al. to visualize the melt fronts to get insight into the melting of triangular energy directors [7,22] and to understand the melting process for film energy directors [5].
- the feedback data of the welder, e.g. time, power, energy and vertical sonotrode displacement. The welding energy and the vertical sonotrode displacement have been related to the weld quality [5,8,23].
- the effect of the welding parameters, i.e. among others welding force, vibrational amplitude, and vibration time, on the welding process. In the static welding process, changing the welding parameters force and vibrational amplitude was found to influence the optimum weld duration significantly [5,8,23]. The welding force affects the degree of hammering of the sonotrode on the top adherend [11,24]. A high welding force reduces the hammering, which makes the process more energy efficient and hence faster. The vibrational amplitude is directly linked to the viscoelastic heat generation  $\dot{Q}_v$  through the following Eq. (1) [25],

$$\dot{Q}_v = \frac{\omega \cdot E'' \cdot \epsilon^2}{2} \quad (1)$$

where  $\omega$  is the frequency of the vibrations,  $E''$  the loss modulus of the material, and  $\epsilon$  the cyclic strain imposed on the material due to the mechanical vibration. Therefore, the amplitude has a major impact on the duration of the welding process.

With the aim of identifying how to benefit from existing knowledge on static ultrasonic welding of thermoplastic composite parts to boost the development of the continuous version of the process, the present paper focuses on identifying and understanding differences and similarities between both processes. To this end, we experimentally compared melting of the interface, the consumed power, temperature at the weld interface, and the optimum welding conditions. This was done for three combinations of welding force and vibrational amplitude which are known to have a significant effect in both welding processes.

## 2. Experimental procedures

### 2.1. Materials

The thermoplastic composite laminates used for the welding experiments in this study were made out of carbon fibre fabric (five harness satin weave) impregnated with polyphenylene sulphide powder (CF/PPS semipreg), CF 0286 127 Tef4 43% from Toray Advanced Composites, the Netherlands. The laminates were stacked according to a  $[0/90]_{3s}$  sequence and subjected to a consolidation process in a hot press for 20 min at 320 °C and 1 MPa pressure, which based on previous experience results in defect- and void-free laminates. The consolidated laminates had a size of 580 mm by 580 mm, and a thickness of approximately 1.85 mm. Adherends measuring 220 mm by 101.6 mm were cut from the consolidated laminates for the continuous welding experiments. For the static welding process 15.0 mm by 101.6 mm adherends were cut from the laminates. For both adherend sizes the main apparent fibre orientation was in the 101.6 mm direction. A 0.20 mm-thick woven PPS mesh energy director with 37% open area was used for all experiments to focus heat generation at the welding interface [17]. The PPS woven mesh (product name PPS100) was supplied by PVF GmbH, Germany.

### 2.2. Ultrasonic welding

The continuous ultrasonic welding machine, shown in Fig. 1a, was developed in-house. This machine was used for all the static and continuous ultrasonic welding experiments. It consists of a stiff frame with a X-Y table on a guiding system allowing automatic translation in its x-direction and an off-the-shelf ultrasonic welder from Herrmann Ultrasonics of the type VE20 SLIMLINE DIALOG 6200. The operating frequency of the welder is 20 kHz. The welding train consists of the converter, booster and sonotrode. The maximum operational amplitude of the sonotrode was defined to be 80  $\mu\text{m}$  (peak-to-peak) by the manufacturer. A rectangular sonotrode was used. The contact surface of the sonotrode was 15 mm-wide and 30 mm-long. In all the experiments carried out in this research, the sonotrode was oriented with its shorter side parallel to the direction in which the X-Y table automatically moved during the welding process (x-direction in Fig. 1a). The ultrasonic welder records feedback data (such as time, power consumption, energy, vertical sonotrode displacement, and amplitude) at a 1 kHz frequency.

Fig. 1b shows a close-up of the continuous ultrasonic welding set-up during the welding process. The CF/PPS top and bottom adherends were kept in place by two aluminium bar clamps placed 70 mm apart from each other. The mesh energy director was placed in between the two adherends. In order to consistently ensure a fixed overlap width of 12.7 mm between the two adherends, alignment pins were used. During the welding process the X-Y table moved underneath the sonotrode in x-direction over a welding distance of 205 mm as shown in Fig. 2, while the sonotrode applied the static welding force and the high-frequency vibrations. The resulting relative movement of the sonotrode with respect to the adherends is indicated in Fig. 1b. The parameters of the continuous welding process were force, amplitude and translational speed.

Fig. 3 shows how the top and bottom adherends for the static welding process were clamped. The same welding machine and clamping tools were used as in the continuous welding set-up (see Fig. 1). For the static welding process, the adherends had the same width as the sonotrode (15 mm). The static welding process was controlled using the vibration time i.e. the welder was set to vibrate for a set amount of time. The welding force and the vibrational amplitude were kept constant for each weld. After the vibration phase a consolidation force equal to the welding force was kept on the adherends by the sonotrode for 4000 ms.

Three combinations of welding force and vibrational amplitude were used for both static and continuous welding processes, shown

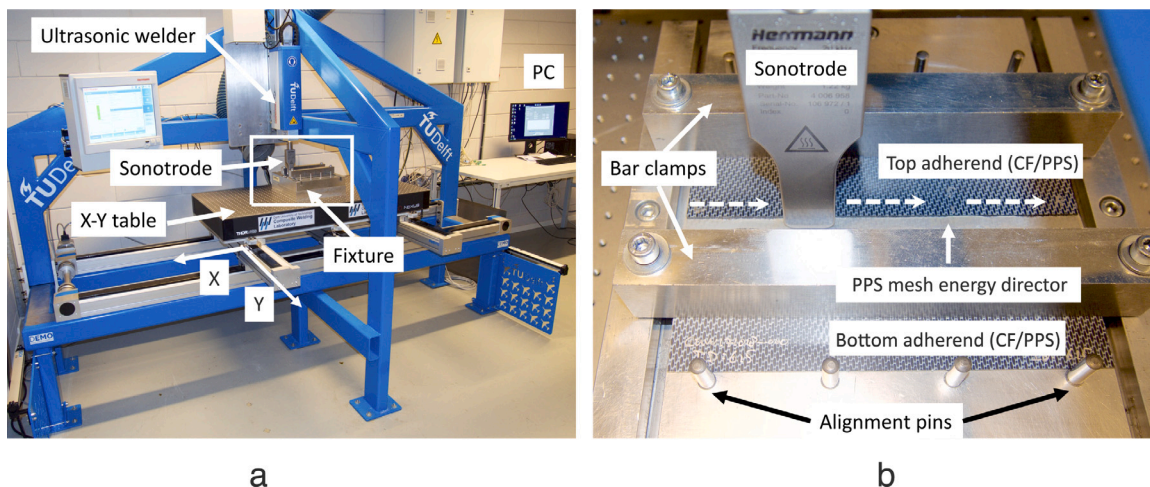


Fig. 1. (a) In-house developed continuous ultrasonic welding machine and (b) a close-up of the to be welded parts together with the sonotrode and the bar clamps.

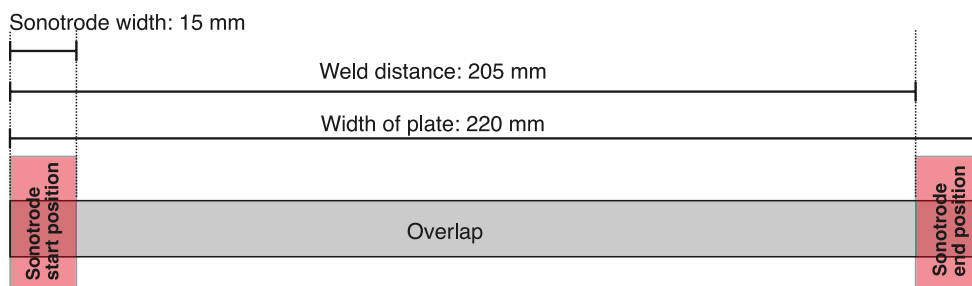


Fig. 2. Schematic overview of start and end position of the sonotrode with respect to the to be welded overlap together with the welding distance.

**Table 1**  
Test matrix for the static and continuous ultrasonic welding experiments for the three parameter combinations with different welding forces (F) and (peak-to-peak) vibrational amplitudes (A).

Parameters combination		Continuous welding	Static welding
F [N]	A [μm]	Speed [mm/s]	Vibration time [ms]
500	80	25	160, 200, 240, 290, 315,
		35	340, 365, 390, 415, 440,
		45	465, 515, 565
1500	80	35	110, 135, 160, 185, 210,
		45	235, 260, 285, 310, 335,
		55	385, 435
500	60	15	500, 600, 675, 800, 865,
		19	915, 940, 965, 1000
		25	

in Table 1. For each combination of force and vibrational amplitude several welding speeds (continuous process) and several vibration times (static process) were used as listed in Table 1.

2.3. Melt front analysis

To understand how the interface melts and to identify the location of the melt front for the continuous welding process a fractographic analysis was performed around the melt front. The location of the melt front was defined as the location from where the melted ED connected to the adherends. The continuous welding process was stopped prematurely at three different weld distances of 56 mm, 100 mm and 144 mm of the leftmost end of the overlap to check for consistency over the length of the plate (see Fig. 2 for reference). For each weld distance one continuous weld was made on an individual set of (top and bottom) adherends until that weld distance was reached. This was done for each combination of welding force and vibrational amplitude (see Table 1) at the optimum welding speed. The welding speed used

was defined as optimum from the results of regular single lap shear tests, as explained later on in Section 3.1. For each weld distance a 50 mm-wide sample was cut from the location where the process was stopped. Each of these samples were mechanically separated, and the resulting fracture surfaces were analysed using a ZEISS Discovery.V8 SteREO microscope. For the close-up image of the mesh a Keyence VR one-shot 3D (VR-5000) microscope was used.

To visualize the melting process during the static ultrasonic welding, four welds in a single lap shear configuration were welded for each combination of welding force, vibrational amplitude, and vibration time indicated in Table 1. These welds were then mechanically tested, and their fracture surfaces were analysed using the ZEISS Discovery.V8 SteREO microscope.

2.4. Energy and power consumption

The areal energy density and average consumed power were determined based on the feedback data from the welder. For the continuous

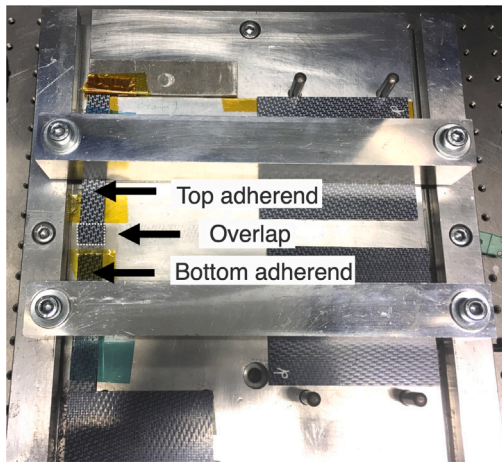


Fig. 3. Clamping situation of adherends in static ultrasonic welding set-up.

process the optimum welding speed was used, and for the static welding process the optimum vibration time was used. For both processes the power curve was integrated with respect to time in order to obtain the consumed energy. The energy density per unit area was determined by dividing the total consumed energy by the total welded area. For the static welding process an average was taken over four welds. For the continuous process the consumed energy and the average power were determined based on the entire welded seam minus the first 15 mm since this area contained non-welded ED.

2.5. Temperature measurements

Fig. 4 shows where the thermocouples were placed for (a) the continuous and (b) the static welding process. The thermocouples were placed in between the bottom adherend and energy director. The temperature at the weld interface was measured using K-type thermocouples supplied by Tempco (product number 2-2200-0004 and description GG220-2K-0). An analog output K-type thermocouple amplifier was used from Adafruit with product number AD8495 sampling the temperature at 1 kHz. The thermocouples had a wire diameter of 0.10 mm. A 25 moving average filter (using the filter function in matlab) was applied to the measured temperature data in order to filter high frequency fluctuations.

For the continuous process 5 evenly spaced thermocouples were placed along the overlap as indicated in Fig. 4. The same welded

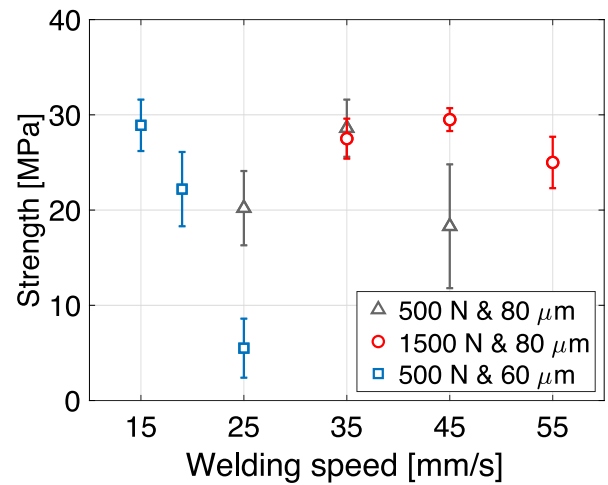
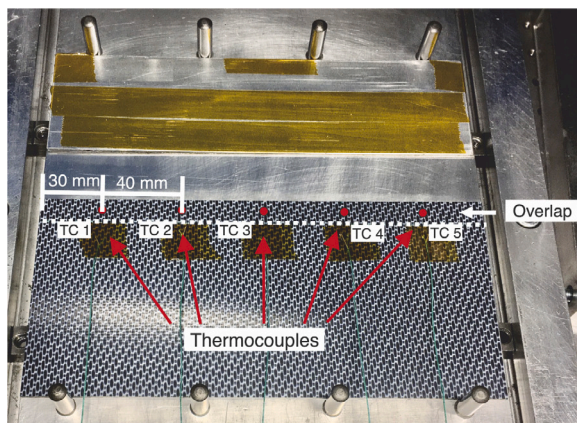


Fig. 5. Average single lap shear strength values obtained after mechanical testing for the continuous ultrasonic welding process. The bars represent plus and minus the standard deviation around the average (n = 6).

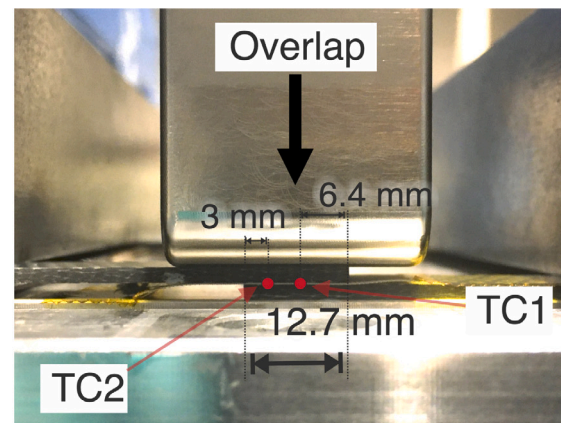
adherends were used for mechanical testing. For the static welding process, 5 additional welds with thermocouples were made for each combination of force and vibrational amplitude, on top of the welds used for mechanical testing. The temperature of the weld interface was measured from the start of the welding process until the optimum vibration time. Per weld two thermocouples were placed, one (TC1) in the middle of the overlap and a second one (TC2) approximately 3 mm from the edge as shown in Fig. 3b.

2.6. Mechanical testing

The continuously welded 220 mm-long adherends were cut into six 25.4 mm-wide single lap shear samples for mechanical testing to obtain their LSS (lap shear strength), after discarding the two edges (28.8 mm-wide each). For the static welding process four welds were made per vibration time for LSS-testing. The obtained single-lap shear samples from both the continuous and static welding processes were mechanically tested with a Zwick/Roell 250 kN universal testing machine with a cross-head speed of 1.3 mm/min. The grips were given the necessary offset to ensure parallelism between the load introduction and the overlap. The LSS was calculated by dividing the maximum load by the overlap area.



a



b

Fig. 4. (a) Bottom adherend in the continuous ultrasonic welding set-up together with five thermocouples. (b) Side view of adherends for static welding with thermocouple locations.

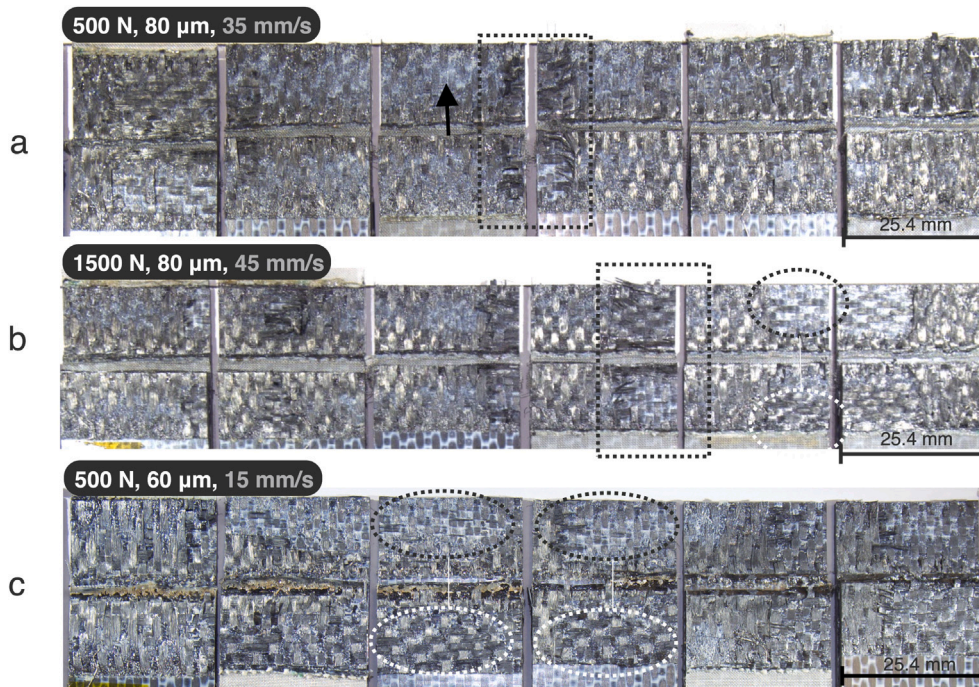


**Fig. 6.** Fracture surfaces of adherends welded at the optimum welding speeds for the three combinations of welding force and vibrational amplitude. The arrow indicates a resin rich area containing voids. The dashed rectangular boxes indicate examples of failures that occurred in between the first and second layer of the bottom adherend. The circle combinations indicate where the first layer of the top adherend separated from the top adherend and remained adhered to the bottom adherend.

### 3. Results

#### 3.1. Mechanical tests

Fig. 5 shows the results of the single lap shear tests of the welded joints obtained by means of the continuous welding process. It should be noted that each point in the graph represents the average strength of six samples cut from a panel welded under a specific combination of force, amplitude and welding speed values. It can be seen that the highest strength values obtained were around 28 MPa for all three force and amplitude combinations. It can also be seen that the optimum welding speed for the 500 N and 80  $\mu\text{m}$  combination was approximately 35 mm/s, which was hence considered as the optimum welding speed for these conditions. A significant drop in strength occurred at either 25 mm/s and 45 mm/s. Increasing the welding force to 1500 N, while maintaining the amplitude constant (80  $\mu\text{m}$ ) resulted in the highest lap shear strength being reached at both 35 and 45 mm/s. It should be noted that according to ANOVA statistical analysis the average lap shear strength values obtained for those two speeds are not statistically different ( $p$ -value = 0.0709 being not significant at  $p < 0.05$ ,  $F = 4.08$ ). However, since degradation of the top adherend was observed when welding at 35 mm/s, 45 mm/s was chosen as the optimum speed for this force and amplitude combination. When increasing the speed to 55 mm/s the strength decreased slightly. For the 500 N and 60  $\mu\text{m}$  combination the optimum welding speed was approximately 15 mm/s. Above a welding speed of 15 mm/s the strength dropped. Below 15 mm/s severe thermal degradation of the top adherend was observed, and thus 15 mm/s was chosen as the lower limit for the speed in this case.

Fig. 6 shows representative fracture surfaces of welds obtained at the optimum welding speed for each one of the three force and amplitude combinations. The fracture surfaces have a uniform appearance and no non-welded energy director was present for any of the welds. However, whitish resin-rich areas containing voids could be observed for all welds. Failure at the weld interface was the most frequent failure type for the 500 N and 80  $\mu\text{m}$  and 1500 N and 80  $\mu\text{m}$  combinations.

However, some of the failure partially occurred in between the first and second layer of the bottom adherend. For the lowest vibrational amplitude (500 N and 60  $\mu\text{m}$  combination), the failure most frequently occurred within the adherends with most of the first ply of the top adherend remaining adhered to the top adherend after failure.

Fig. 7 shows the lap shear strength values corresponding to the static welding process. For the 500 N and 80  $\mu\text{m}$  combination, the strength gradually increased to an interval of high strength values (around 36 MPa) for vibration times between 415 ms and 565 ms. When increasing the welding force to 1500 N and keeping the vibrational amplitude at 80  $\mu\text{m}$ , the high strength interval (also around 36 MPa) was achieved within a shorter vibration time, between 260 ms and 435 ms. When lowering the vibrational amplitude to 60  $\mu\text{m}$  while keeping the welding force at 500 N, the high strength interval (around 38 MPa) was reached significantly later, at vibration times between 860 ms and 960 ms. The optimum vibration times were determined within these high strength intervals based on fractographic analysis. The optimum vibration time was identified as the shortest vibration time within the said interval for which no non-welded energy director could be observed anymore: 440 ms for 500 N and 80  $\mu\text{m}$ , 335 ms for 1500 N and 80  $\mu\text{m}$ , and 940 ms for 500 N and 60  $\mu\text{m}$ .

#### 3.2. Power and displacement curves

Fig. 8 shows the power and displacement curves in the continuous ultrasonic welding process at the optimum welding speeds. For all combinations of welding force and vibrational amplitude the power quickly increased at the start of the welding process. Throughout the welding process the power fluctuated around an average power value of approximately 1600 W for 500 N & 80  $\mu\text{m}$  (Fig. 8a), 1900 W for 1500 N & 80  $\mu\text{m}$  (Fig. 8b), and 900 W for 500 N & 60  $\mu\text{m}$  (Fig. 8c). The power fluctuations near the start and end of the weld were bigger compared to those in the middle. Overall, the power fluctuations were less pronounced for the 500 N & 60  $\mu\text{m}$  case (Fig. 8c). The vertical displacement of the sonotrode did not show a consistent behaviour.

Fig. 9 shows the power and displacement curves of the static ultrasonic welding process for the three different combinations of welding

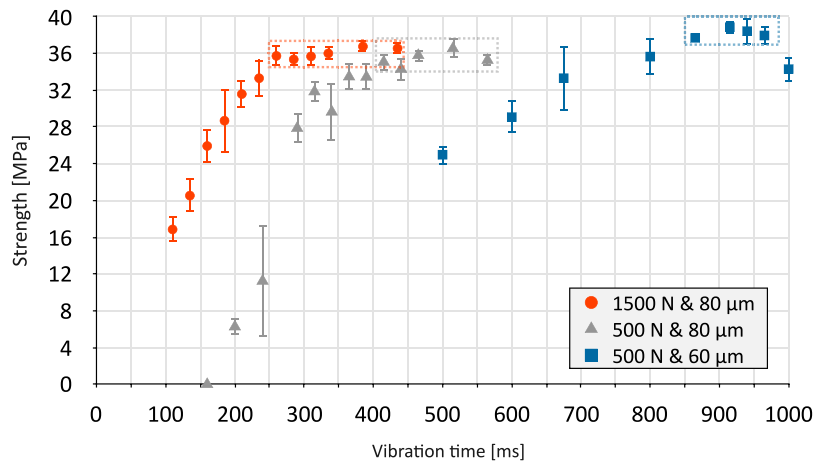


Fig. 7. Average single lap shear strength obtained after mechanical testing of the samples statically welded at different vibration times. The bars represent plus and minus the standard deviation around the average (n = 4).

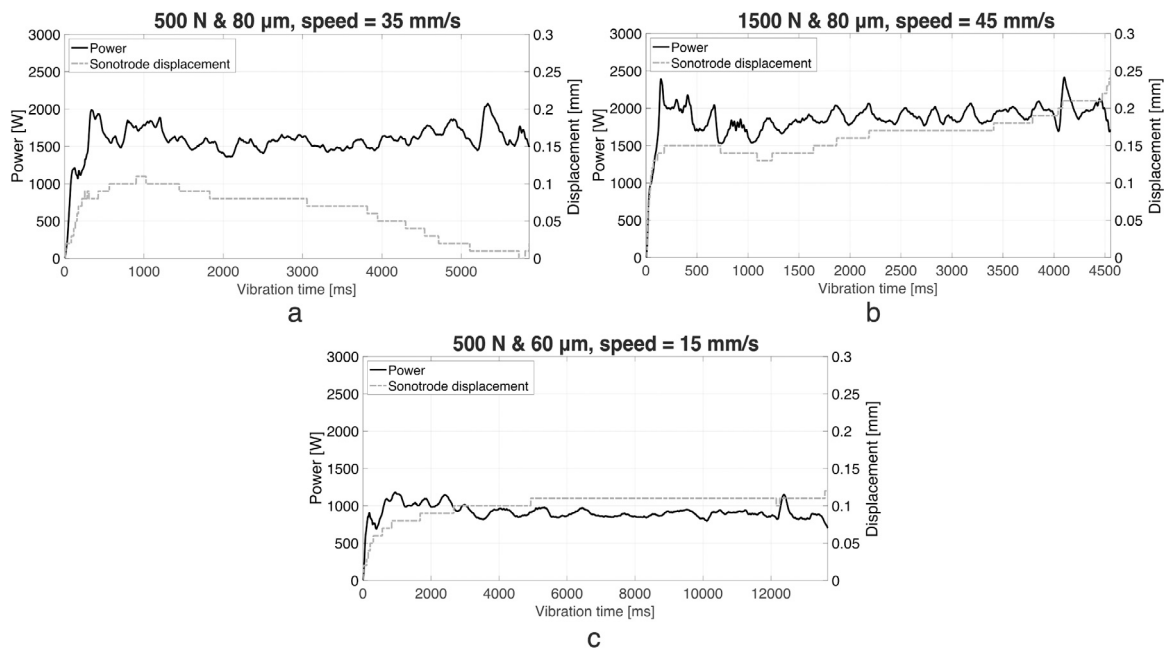


Fig. 8. Power and vertical sonotrode displacement curves of the continuous ultrasonic welding process for the three combinations of force and vibrational amplitude welded at the optimum welding speed.

force and vibrational amplitude. As seen in Fig. 9a, b, and c, in all cases the power steeply increased within the first 100 ms. The steepest power increase occurred for the 1500 N & 80 μm combination (Fig. 9b), followed by the 500 N & 80 μm (Fig. 9a) and the 500 N & 60 μm combinations (Fig. 9c). After the initial increase the power remained between approximately 800 W and 1500 W for the 500 N & 80 μm combination (Fig. 9a), between 1200 W and 1800 W for the 1500 N & 80 μm combination (Fig. 9b), and between 500 W and 800 W for the 500 N & 60 μm combination (Fig. 9c).

The vertical displacement in Figs. 9a, 9b, and 9c increased steeply within 130 ms (500 N & 80 μm), 50 ms (1500 N & 80 μm), and 220 ms (500 N & 60 μm) respectively. This initial step increase was followed by a plateau in displacement, lasting approximately 80 ms for 500 N & 80 μm, 60 ms for 1500 N & 80 μm, and 240 ms for 500 N & 60 μm.

### 3.3. Melt front analysis

Fig. 10 shows representative fracture surfaces where the continuous welding process was prematurely stopped at 100 mm from the leftmost

edge of the overlap for the three combinations of force and vibrational amplitude and optimum welding speeds. As shown in Fig. 10a, b, and c, in all three cases the melt front was underneath the sonotrode, was relatively straight, parallel to the back and front edge of the sonotrode and closer to the latter. Behind the melt front (i.e. the welded area), rough resin-rich surface with occasional broken fibres (see Fig. 10a, b, and c) could be observed. The whole energy director and presumably the resin on the outer surface of the adherends had been melted. Ahead of the melt front non-welded energy director was present. Fig. 10d shows a close-up of a part of the non-welded energy director under and ahead of the sonotrode. It can be seen that close to the melt front the ED was significantly deformed and flattened, the degree of deformation and flattening decreased towards fully pristine ED far ahead of the sonotrode.

In Fig. 10 the position of the melt front was dependent on the process parameters. Table 2 shows the position of the melt front relative to the front edge of the sonotrode (referred to as melt front distance) and the position of the melt front relative to the pristine ED at three different positions in the overlap for each combination of processing

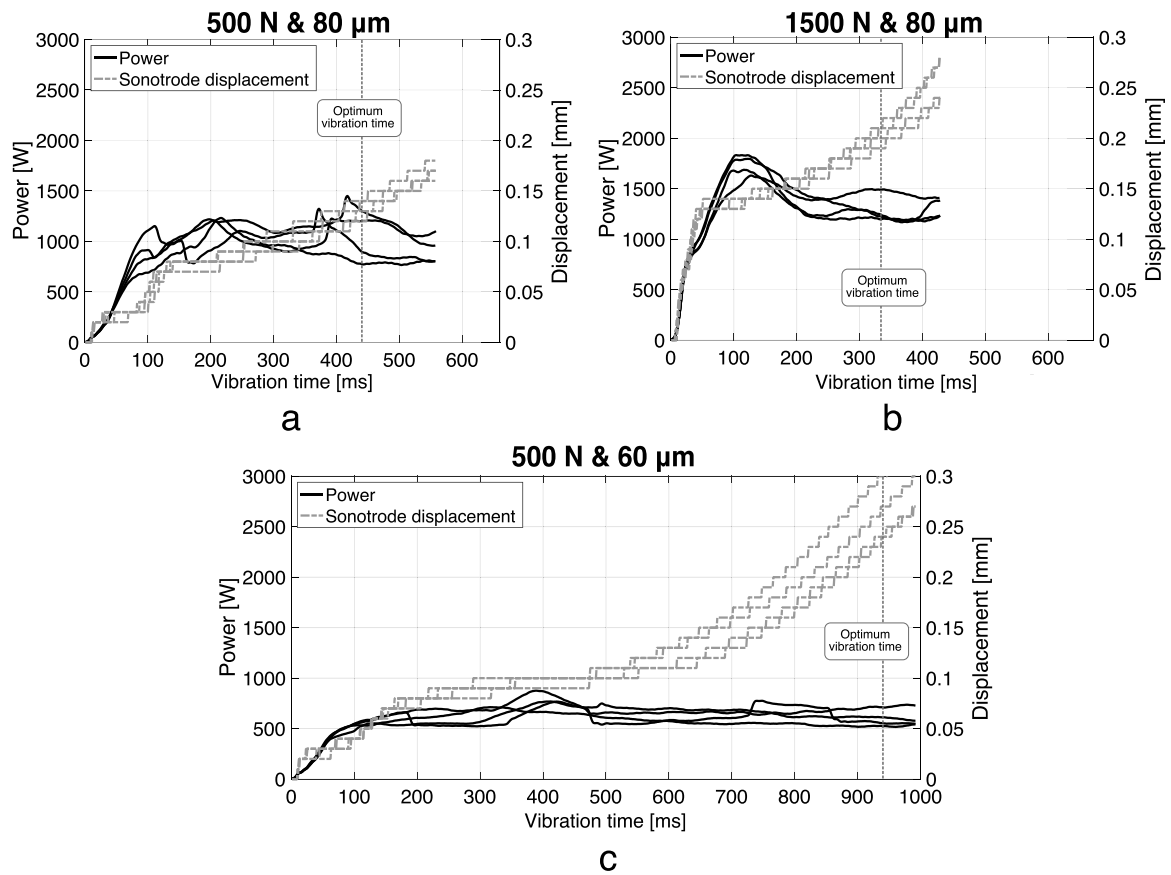


Fig. 9. Power and vertical sonotrode displacement curves of the static ultrasonic welding process for the three combinations of force and vibrational amplitude.

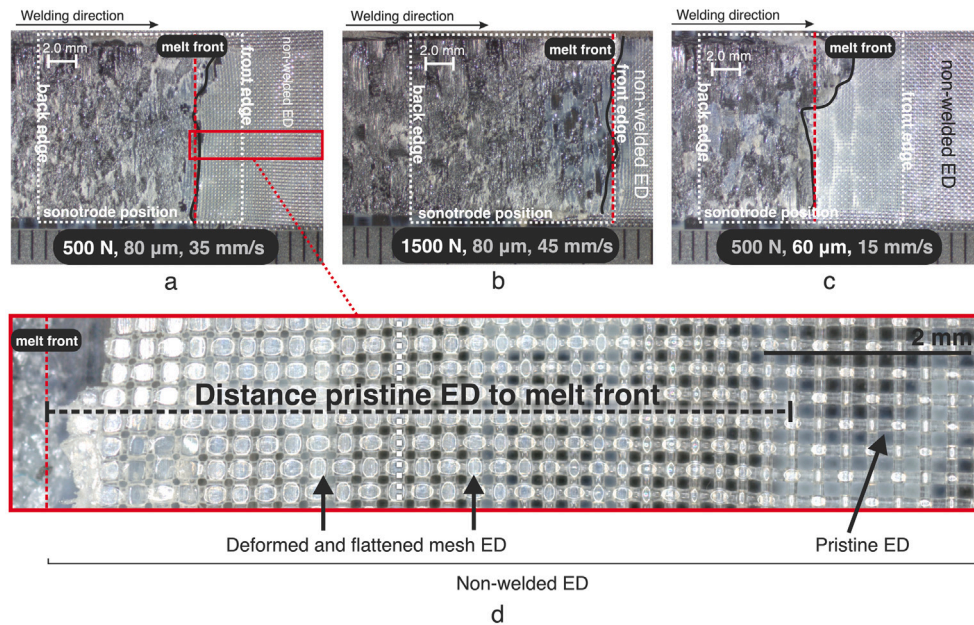


Fig. 10. Representative fracture surfaces showing the melt front positions at optimum welding speeds after stopping the welding process at 100 mm from the leftmost edge of the overlap for (a) 500 N, 80 μm and 35 mm/s, (b) 1500 N, 80 μm, and 45 mm/s, (c) 500 N, 60 μm, and 15 mm/s. The white dashed rectangles mark the position of the sonotrode when the welding process was stopped. The front edge and the back edge of the sonotrode are also indicated. (d) Close-up of mainly the non-welded energy directing mesh ahead of sonotrode. The distance between the pristine ED and the melt front is shown.

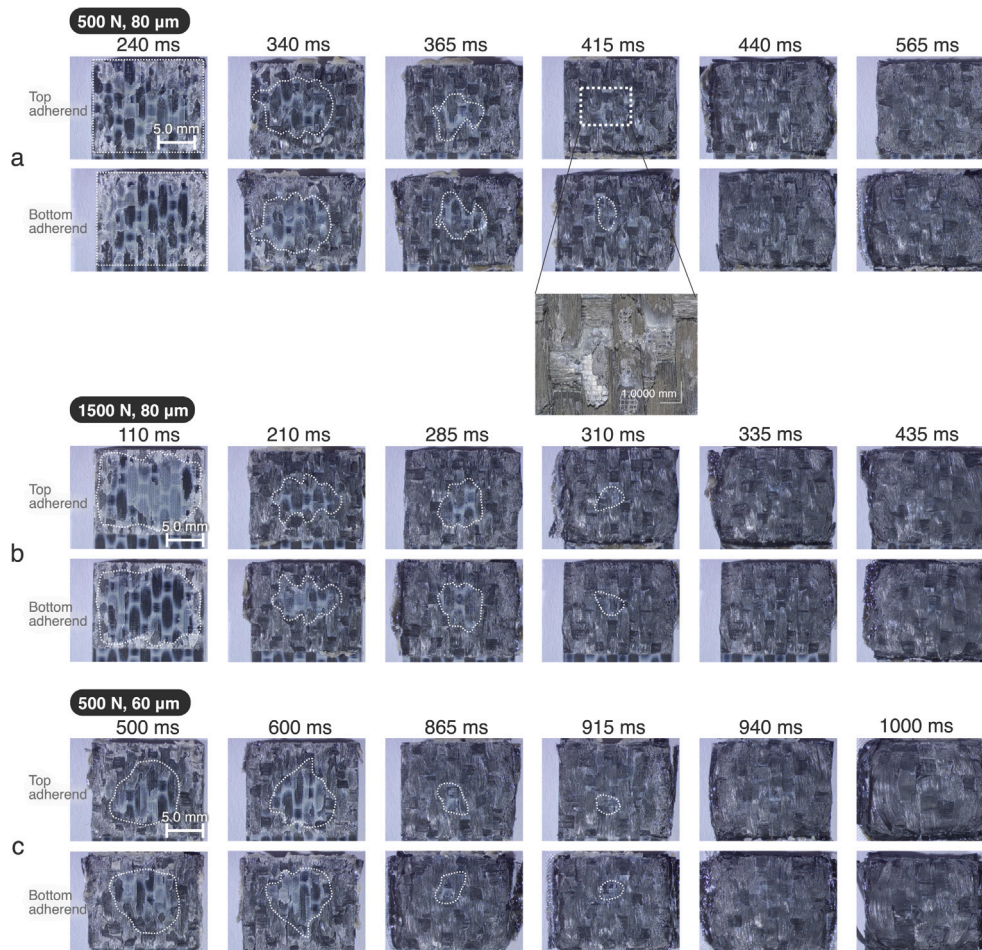
parameters (see Section 2.3). It can be seen that the melt front distance remained relatively constant during the welding process with the largest standard deviation found for the 500 N and 60 μm combination.

Fig. 11 shows representative fracture surfaces of adherends statically welded under different vibration times for the three combinations of welding force and vibrational amplitude used in this study. It can be seen that for each combination of welding parameters the centre of

**Table 2**

Average melt front distances with respect to the front edge of the sonotrode and position of melt front relative to the pristine ED for the three combinations of welding force (F) and vibrational amplitude (A) welded at the optimum welding speeds (S).

Parameters			Avg. melt front distance to front edge sonotrode [mm]	Avg. position melt front relative to pristine ED [mm]
F [N]	A [ $\mu\text{m}$ ]	S [mm/s]		
500	80	35	$3.2 \pm 0.6$	$6.2 \pm 0.4$
1500	80	45	$0.5 \pm 0.5$	$4.3 \pm 0.7$
500	60	15	$6.0 \pm 0.9$	$8.2 \pm 1.7$



**Fig. 11.** Representative fracture surfaces of statically welded adherends at multiple different vibration times for the three combinations of welding force and vibrational amplitude: 500 N and 80  $\mu\text{m}$ , 1500 N and 80  $\mu\text{m}$ , and 500 N and 60  $\mu\text{m}$ . The white dashed areas indicate the presence of non-welded energy director.

the overlap melted the latest. The area of non-welded energy director material decreased for increased vibration times. The first vibration times for which the welds contained no non-welded energy director are 440 ms for 500 N and 80  $\mu\text{m}$ , 335 ms for 1500 N and 80  $\mu\text{m}$ , and 940 ms for 500 N and 60  $\mu\text{m}$ . For most of the welds obtained under vibration times beyond those values fibre distortion could be observed at the edges of the overlap.

**3.4. Power, energy and temperature measurements**

Table 3 shows the areal energy density and the average consumed power for both the static and continuous welding processes at the optimum vibration time and welding speed, respectively. It can be seen that energy and power were significantly higher for the continuous welding process. The difference was most pronounced for the 500 N and 80  $\mu\text{m}$  parameter combination, where both the average power and

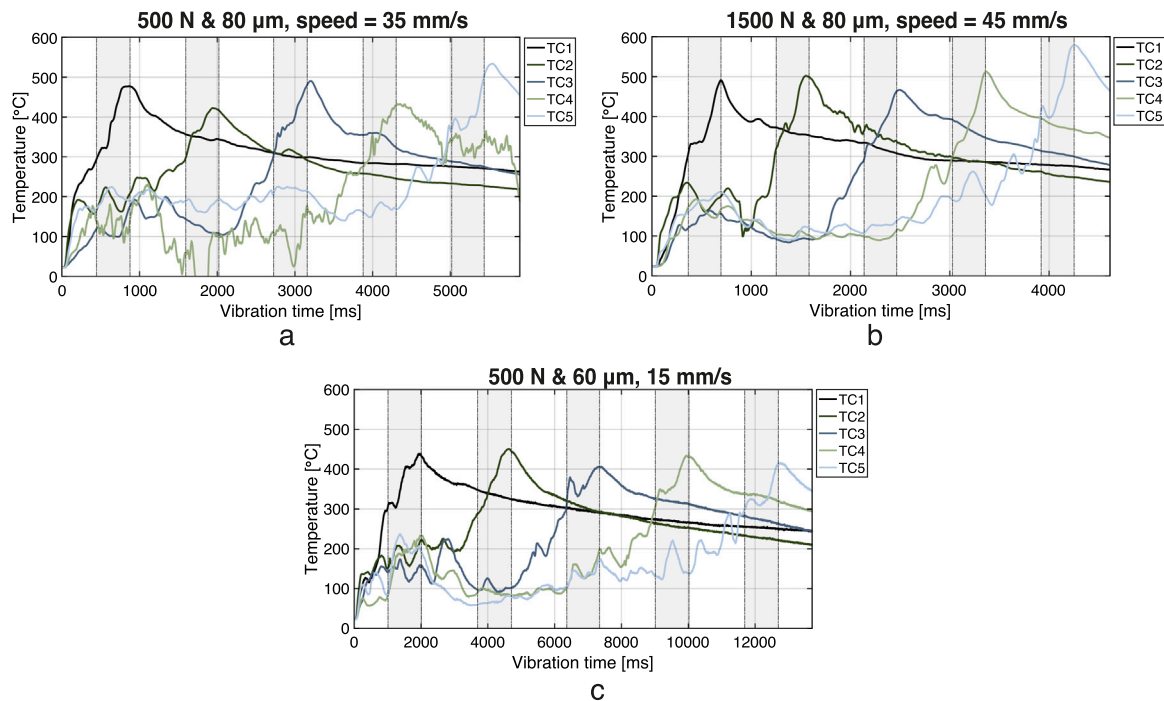
the energy density in continuous ultrasonic welding were almost twice as high as those of the static welding process. The smallest difference occurred for the 1500 N and 80  $\mu\text{m}$  parameter combination, with the power and energy being 1.4 times higher in continuous than in static welding.

Fig. 12 shows the temperatures measured during the continuous welding process at five different locations in the welding interface (see Section 2.5). The grey shaded areas indicate the time span during which a specific thermocouple was located under the sonotrode. It can be seen that the temperature measured by all the thermocouples increased almost instantly to values between 100 °C and 200 °C at the beginning of the welding process. Afterwards, the temperature started to increase more steeply well before the sonotrode reached the thermocouple until a maximum value was reached coinciding with the point where the sonotrode moved away from the thermocouple. The maximum temperatures were  $474 \text{ }^\circ\text{C} \pm 45 \text{ }^\circ\text{C}$ ,  $512 \text{ }^\circ\text{C} \pm 41 \text{ }^\circ\text{C}$ , and

**Table 3**

Average power and average areal energy density and corresponding standard deviation for the three combinations of force and vibrational amplitude welded at the optimum static vibration times and optimum continuous welding speeds.

combination	Technique	Optimum	Areal energy density [J/mm <sup>2</sup> ]	Average power [W]
500 N, 80 $\mu$ m	Static	440 ms	1.9 $\pm$ 0.1	843 $\pm$ 41
	Continuous	35 mm/s	3.6 $\pm$ 0.3	1605 $\pm$ 131
1500 N, 80 $\mu$ m	Static	335 ms	2.4 $\pm$ 0.1	1352 $\pm$ 60
	Continuous	45 mm/s	3.3 $\pm$ 0.2	1869 $\pm$ 135
500 N, 60 $\mu$ m	Static	940 ms	2.9 $\pm$ 0.3	588 $\pm$ 54
	Continuous	15 mm/s	4.8 $\pm$ 0.4	916 $\pm$ 76



**Fig. 12.** Representative temperature measurements for the continuous ultrasonic welding process at the optimum welding speeds for the three parameter combinations. The grey areas indicate the time span during which a specific thermocouple was located under the sonotrode.

433  $\pm$  17  $^{\circ}$ C for 500 N & 80  $\mu$ m (Fig. 12a), 1500 N & 80  $\mu$ m (Fig. 12b), and 500 N & 60  $\mu$ m (Fig. 12c), respectively.

Fig. 13 shows representative temperature measurements at the welding interface for the static ultrasonic welding process. Temperature measurements both at the centre and at one of the edges of the overlap (see Section 2.5) are represented in this Figure. As seen in Fig. 13a, b, and c, in all cases the temperature evolution showed a first stage in which it increased quickly from room temperature to over the melting temperature of PPS (280  $^{\circ}$ C [26]) within the first 50 to 100 ms of the process (50 ms for 1500 N & 80  $\mu$ m and 100 ms for 500 N & 80  $\mu$ m and 500 N & 60  $\mu$ m). After that, a second stage could be observed in which the temperature increase rate slowed down significantly. The duration of this second stage was also between 50 and 100 ms. Temperatures at the centre and at the edge of the overlap were similar during these first and second stages. After that, the temperatures at both locations still showed increasing trends but tended to diverge from each other. While for the 1500 N & 80  $\mu$ m (Fig. 13b) and the 500 N & 60  $\mu$ m (Fig. 13c) combinations, the temperature at the edge of the overlap was generally higher than at the centre, for the 500 N & 80  $\mu$ m combination (Fig. 13a) the opposite behaviour was observed. For the 500 N & 80  $\mu$ m combination the maximum temperature amounted to around 450  $^{\circ}$ C (centre of the overlap). For the 1500 N & 80  $\mu$ m combination the maximum temperature was around 550  $^{\circ}$ C (edge of the overlap). Finally, for the 500 N & 60  $\mu$ m combination the maximum temperature was around 500  $^{\circ}$ C (edge of the overlap).

#### 4. Discussion

The aim of this paper was to identify and understand differences and similarities between the static and continuous ultrasonic welding processes for thermoplastic composites. In particular, melting of the interface, consumed power and energy density, temperature evolution at the weld interface, and optimum welding conditions for both types of processes were investigated. This was done for three combinations of welding force and vibrational amplitude, parameters which are known to have a significant effect in both welding processes. Our interpretation of the results obtained in this study is provided in what follows.

Regarding melting of the interface, the fracture surfaces in Figs. 10 and 11 show a fundamental difference between the continuous and the static welding process. While in the static process the amount of non-welded area gradually decreases until it becomes zero, in the continuous process the amount of non-welded area under the sonotrode remains constant. In other words, in static welding the condition of the material under the sonotrode gradually changes, as it sequentially undergoes all the stages in the welding process. Contrarily, an unchanging condition (a simultaneous combination of the different stages the material goes through during the welding process, as schematically represented in Fig. 14) can be found under the sonotrode in the continuous welding process. The amount of non-welded area under the sonotrode in the continuous process is reduced when either the

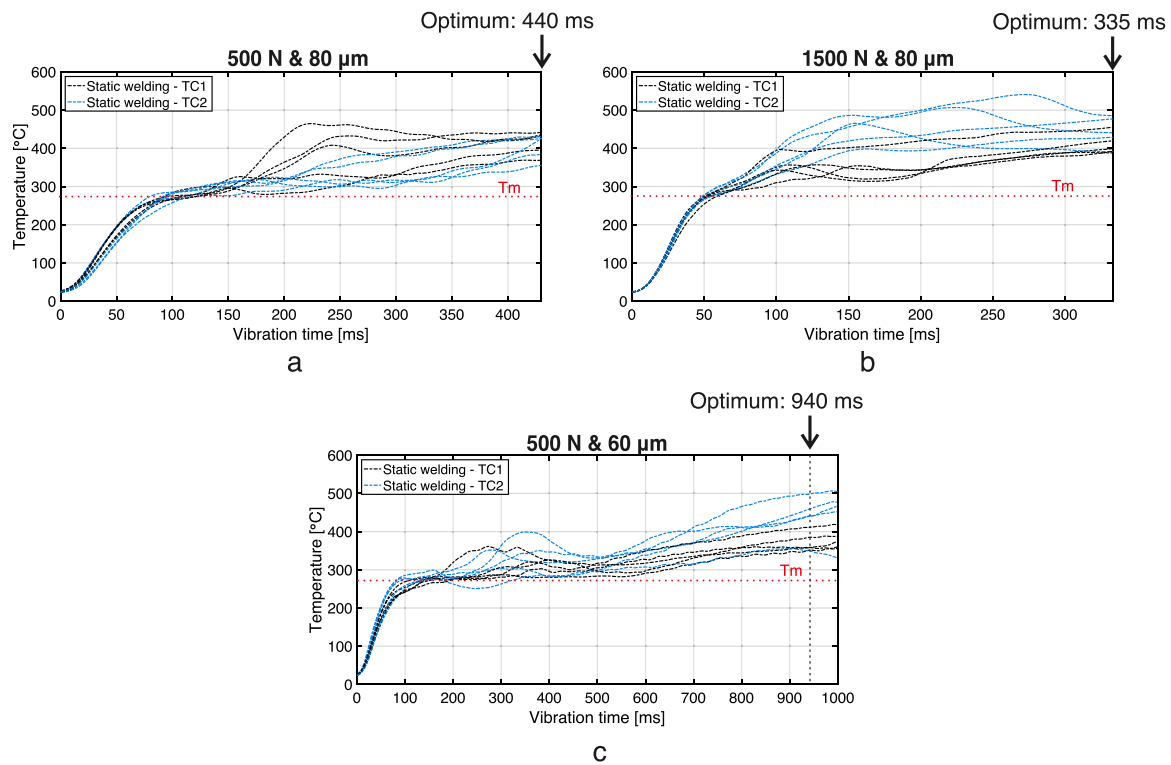


Fig. 13. Representative temperature measurements for the static welding process until the optimum vibration time for the three parameter combinations. TC1 was located in the centre of the overlap and TC2 was located on the edge of the overlap as indicated in Fig. 4b.

welding force or amplitude increase (Fig. 10). This is consistent with faster heat generation and hence a shorter time for the non-welded energy director to turn into a welded joint. When it comes to the power dissipated during the welding process, the morphology of the power curves is similar in both processes (Figs. 8 and 9). They feature an initial rapid increase followed by fluctuations around a certain value, which are believed to represent the different phases undergone by the material. However, the overall dissipated power as well as the energy density are significantly higher in the continuous process (see Table 3). We believe this is related to the differences in adherend size since, as widely acknowledged in literature, the power or energy in ultrasonic welding is not only invested in creating the weld but also dissipated in its surroundings. As a matter of fact, additional experiments in which a 15 mm-wide static weld was made at the centre of 220 mm-wide adherends (same adherend and energy director configuration as in continuous welding) showed power dissipation levels comparable to those observed in continuous welding (Fig. 15).

Higher power dissipation when the adherends are wider than the sonotrode (i.e. continuous versus static welding situations in this study) may be explained by two phenomena. Firstly, by the vibrations being transmitted beyond the material directly underneath the sonotrode. As shown in Fig. 12, all the thermocouples registered a rather simultaneous temperature increase to a temperature level between 100 and 200 °C at the beginning of the continuous process. Such phenomenon can be interpreted as resulting from the occurrence of vibration and hence friction between the thermocouples and adherends all along the overlap and not only at the specific location of the sonotrode. Secondly, by the initial phases of the welding process occurring beyond the boundaries of the sonotrode. As seen in Fig. 10, the mesh energy director experiences local melting and flattening ahead of the sonotrode in the continuous process. Additionally, the temperature at each thermocouple location starts the ramp-up associated with the welding process before the sonotrode arrives at that location (Fig. 12). Therefore, owing to pressure distribution and amplitude transmission beyond the sonotrode, the effective area undergoing the different stages

of the welding process can be said to be bigger than the actual imprint of the sonotrode, which results in higher power needs.

As mentioned earlier, in continuous welding the temperature starts ramping up beyond the pseudo-initial 100–200 °C level before the sonotrode reaches each location. This is obviously not the case in static welding. However the maximum temperatures reached in both types of process are roughly within the same 150 °C-wide range as seen in Fig. 16. Despite the higher thermal energy input derived from longer exposure to high temperatures in continuous welding, both the continuous and static process show similar melting kinetics at the welding interface. Firstly, the time to transform pristine ED into melted ED connected to the adherends, represented by the distance between the melt front and pristine ED in continuous welding (Fig. 10) and by the time until the end of the displacement plateau in static welding [17], are similar as shown in Table 4. Secondly, the optimum vibration times (static welding) and optimum welding speeds (continuous welding) are also similar (Table 4). This indicates that in the particular case studied here, results from the static process can be used to determine the optimum welding speed in the continuous process. This is an important result since it could lead to a considerable reduction of the effort needed to define optimum welding conditions in continuous ultrasonic welding by making use of the relatively simple and efficient methods available in literature to define the optimum vibration time in the static process [5,8]. Nevertheless, the obvious differences in temperature evolution between the two processes and their potential impact on the validity of the relation between vibration time (static) and welding speed (continuous) need to be further understood. In particular, changing the thermal properties of the adherends and/or the melting behaviour of the energy director by, for instance, welding a different composite material, might challenge the aforementioned relation. On the contrary, introducing changes in the welding setup (ultrasonic welder, clamping jig) could likely result in different absolute values for both the vibration time and welding speed but not in the relation between them. This is supported by the fact that the three force and amplitude combinations used in this study showed a similar

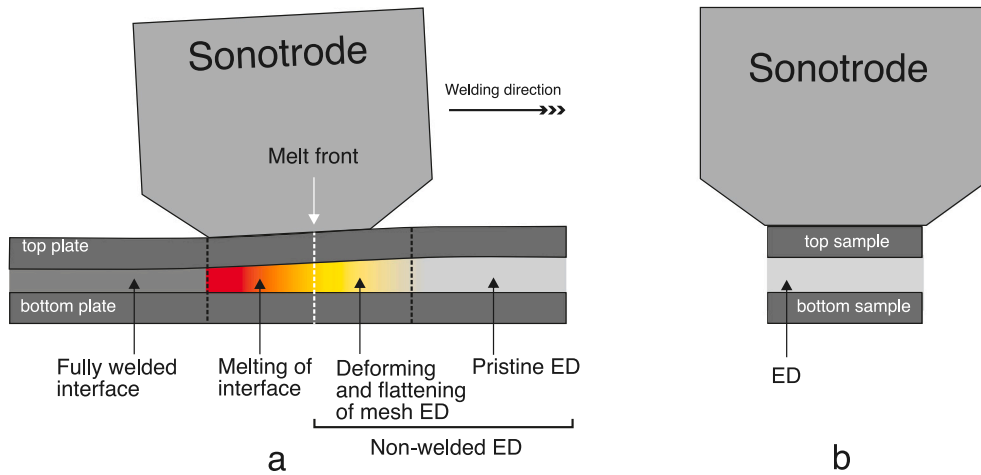


Fig. 14. (a) Schematic exaggerated interpretation of the CUV process at the interface. (b) Schematic situation for the static welding process.

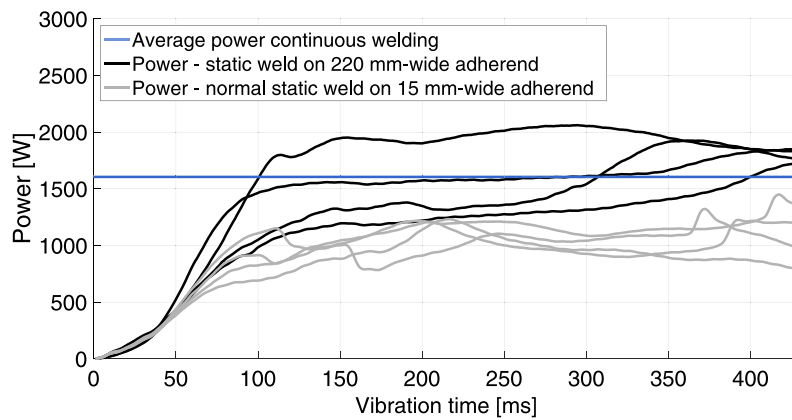


Fig. 15. Power curves for the 500 N & 80  $\mu\text{m}$  combination for a normal static weld on 15 mm-wide coupons as shown in Fig. 3, and a static welds made in the middle of 220 mm-wide adherends normally used for continuous welding.

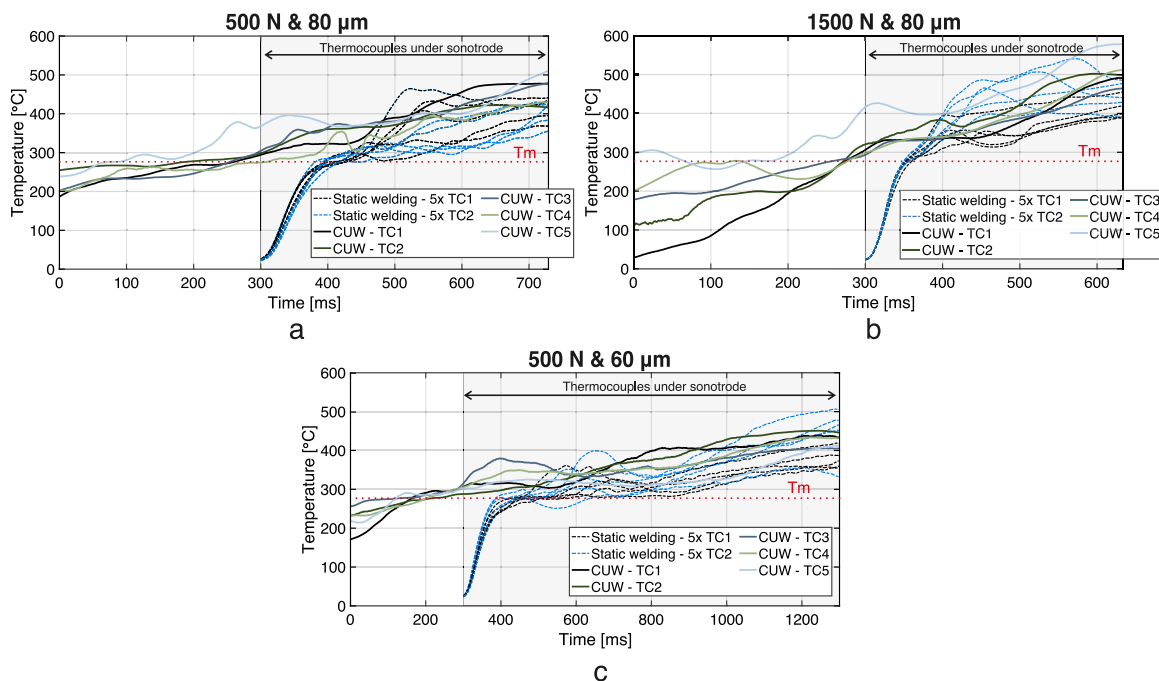
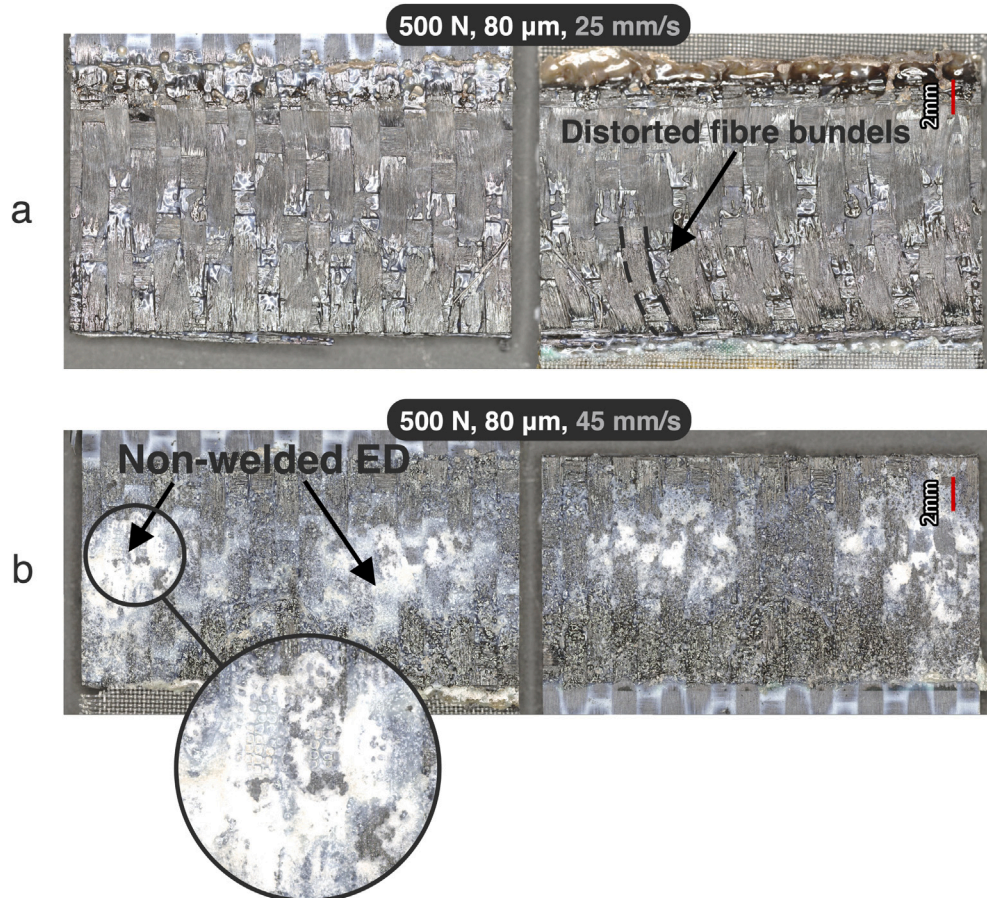


Fig. 16. Representative temperature measurements for the continuous and the static welding process when the thermocouple is directly under the sonotrode (grey shaded area) and 300 ms before shown for the three parameter combinations at the optimum welding speed (continuous) and optimum vibration time (static) respectively.

**Table 4**

Time to transform pristine ED into melted ED for static (time values at the end of the displacement plateaus in Fig. 9) and CUW (calculated by dividing the distance from the pristine ED to the melt front in Table 2 by the corresponding welding speeds). Translation of optimum welding speeds into vibration times for CUW (by dividing the sonotrode width of 15 mm by the optimum CUW speed), and optimum vibration times in static welding identified in Section 3.1.

		500 N and 80 $\mu\text{m}$	1500 N and 80 $\mu\text{m}$	500 N and 60 $\mu\text{m}$
Time to transform pristine ED into melted ED	Static	200 ms	100 ms	490 ms
	CUW	180 ms	100 ms	550 ms
Optimum	Time based on CUW speed	429 ms	333 ms	1000 ms
	Time static	440 ms	335 ms	940 ms



**Fig. 17.** Representative fracture surfaces of continuous welds for the 500 N and 80  $\mu\text{m}$  parameter combination/s obtained at welding speed (a) below and (b) above the optimum welding speed. (a) displays distorted fibre bundles and discoloured resin at the edges of the overlap, (b) shows areas of non-welded ED. Top adherend is shown on the left and bottom adherend is shown on the right.

relation between vibration time and welding speed despite the very different absolute values in each combination.

Finally, the maximum lap shear strength of continuous welded joints is significantly lower than that of statically welded joints. We believe this to be related to the presence of voids weakening the welding interface (main failure location as seen in Fig. 6) and, potentially, the adjacent layers in the adherends (secondary failure location as also seen in Fig. 6). These voids, which could be distinctly observed on the fracture surfaces of the continuous welds (Fig. 6), are believed to be caused by lack of consolidation during the welding process, i.e. no pressure applied during cooling. Lack of consolidation could result from: (i) the continuous welding set-up missing a consolidation shoe which would enable the welded areas to cool down under pressure; (ii) uneven thickness and resulting uneven pressure caused by the presence of non-welded ED under the sonotrode (as indicated in Fig. 14). Owing to the fact that welded joints obtained at 1500 N and 80  $\mu\text{m}$  featured the same maximum LSS as the other welded joints despite the fact that the

melt front was aligned with the front edge of the sonotrode (Fig. 10) points at the absence of a consolidation shoe as the main cause in the LSS knock down. We therefore expect that adding a consolidation shoe to the continuous welding setup will decrease the amount of voids in the weld line and the adherends and will hence increase the strength of the continuous ultrasonic welds to values similar to those of static welds. We however do not expect the optimum welding speeds defined in the present study to be significantly affected by the addition of a compaction shoe to the welding setup. This is based on the fact that the fracture surfaces of samples welded at welding speeds below and above the optimum featured initial signs of overheating (fibre distortion, discoloured resin) and areas of not completely molten ED, respectively (see e.g. Fig. 17). Both overheating and non-molten ED are majorly related to the heating phase of the welding process and, consequently, we do not expect them to be affected by whether consolidation pressure is applied or not during the cooling phase.

## 5. Conclusions

The objective of this paper was to investigate similarities and differences between the static and continuous ultrasonic welding process for thermoplastic composites in order to identify how we can benefit from the available knowledge in static welding to further develop and understand the continuous process. The two processes were compared experimentally with respect to the melting of the interface, the required areal energy density and consumed power, the temperature at the interface, and the effect of changes in welding parameters welding force and vibrational amplitude on the optimum welding conditions. The main conclusions from this study are the following:

- For the continuous process the amount of non-welded area under the sonotrode remains constant, while for the static process the amount of non-welded area gradually decreases until it becomes zero. In other words, for the continuous process there is a constant coexistence of different phases the material goes through. In the static process, on the other hand, the material sequentially undergoes all phases of the welding process.
- The morphology of the power curves is similar for both processes. Both featuring a rapid increase at the beginning followed by fluctuation around a certain value. However, the overall dissipated power for the continuous process is significantly higher. This is most likely caused by the larger adherend size in the continuous process.
- For the continuous welding process the temperature measured at each thermocouple location starts to ramp before the sonotrode arrives at that specific location. Therefore, the effective area undergoing the different stages of the welding process can be said to be bigger than the actual imprint of the sonotrode, which results in higher power needs. Despite the higher power needs for the continuous process both the static and continuous process resulted in maximum temperatures within the same range.
- The optimum vibration times and welding speeds in both processes are similar, indicating that the kinetics of the melting process were not sensitive to whether the process was performed in a static or continuous manner. This similarity has the potential to significantly reduce the labour and material effort invested in defining optimum welding conditions in continuous ultrasonic welding by making use of the relatively simple and efficient methods available in literature to define the optimum vibration time in the static process. Further work is however needed to identify the sensitivity of this conclusion to changes in, for instance, the nature of the composite material being welded.
- The maximum lap shear strength of the continuous welded joints is significantly lower than that of the statically welded joints. This is most likely related to the presence of voids at the continuous welded interface. The voids are believed to be caused by a lack of consolidation during cooling. Therefore, we expect the weld quality and the lap shear strength to increase once a consolidation shoe is implemented into the welding process.

## Declaration of competing interest

The authors declare that they have no known competing financial interests or personal relationships that could have appeared to influence the work reported in this paper.

## Acknowledgements

This study was funded by the European research programme Clean Sky. The ecoTECH project has received funding from the European Union's Horizon 2020 Clean Sky 2 Joint Undertaking under the AIR-FRAME ITD grant agreement 807083.

The authors would like to especially thank Rein van den Oever from the Electronic and Mechanical Support Division from the TUDelft for the electronic and software development of the continuous ultrasonic welding machine. The authors like to thank Perry Posthoorn from the Electronic and Mechanical Support Division from the TUDelft for the mechanical design of the continuous ultrasonic welding machine. Additionally, the authors like to thank Marco Sebastian from Herrmann Ultrasonics for his help to integrate the off-the-shelf welder into our continuous ultrasonic welding machine and for his continuous support and interest in the welding of thermoplastic composites.

## References

- [1] Gardiner G. Thermoplastic composites gain leading edge on the A380. *High-Perform Compos* 2006;14(2):50–5.
- [2] Offringa Arnt. New thermoplastic composite design concepts and their automated manufacture. *JEC Compos Mag* 2010;58:45–9.
- [3] Potente H. Ultrasonic welding - Principles & theory. *Mater Des* 1984;5(5):228–34.
- [4] Zhang Zongbo, Wang Xiaodong, Luo Yi, Zhang Zhenqiang, Wang Liding. Study on heating process of ultrasonic welding for thermoplastics. *J Thermoplast Compos Mater* 2010;23(5):647–64.
- [5] Villegas IF. In situ monitoring of ultrasonic welding of thermoplastic composites through power and displacement data. *J Thermoplast Compos Mater* 2015;28(1):66–85.
- [6] Palardy G, Villegas IF. On the effect of flat energy directors thickness on heat generation during ultrasonic welding of thermoplastic composites. *Compos Interfaces* 2017;24(2):203–14.
- [7] Villegas IF, Valle Grande B, Bersee HEN, Benedictus R. A comparative evaluation between flat and traditional energy directors for ultrasonic welding of CF/PPS thermoplastic composites. *Compos Interfaces* 2015;22(8):717–29.
- [8] Villegas IF. Strength development versus process data in ultrasonic welding of thermoplastic composites with flat energy directors and its application to the definition of optimum processing parameters. *Composites A* 2014;65:27–37.
- [9] Zhao T, Palardy G, Villegas IF, Rans C, Martinez M, Benedictus R. Mechanical behaviour of thermoplastic composites spot-welded and mechanically fastened joints: A preliminary comparison. *Composites B* 2017;112:224–34.
- [10] Villegas IF, Rubio PV. On avoiding thermal degradation during welding of high-performance thermoplastic composites to thermoset composites. *Composites A* 2015;77(Suppl. C):172–80. <http://www.sciencedirect.com/science/article/pii/S1359835X15002341>.
- [11] Levy A, Le Corre S, Villegas IF. Modeling of the heating phenomena in ultrasonic welding of thermoplastic composites with flat energy directors. *J Mater Process Technol* 2014;214(7):1361–71.
- [12] Villegas IF, Bersee H. Ultrasonic welding of advanced thermoplastic composites: An investigation on energy-directing surfaces. *Adv Polym Technol* 2010;29(2):112–21.
- [13] Zhao T, Broek C, Palardy G, Villegas IF, Benedictus R. Towards robust sequential ultrasonic spot welding of thermoplastic composites: Welding process control strategy for consistent weld quality. *Composites A* 2018;109:355–67.
- [14] Koutras N, Amirdine J, Boyard N, Villegas I Fernandez, Benedictus R. Characterisation of crystallinity at the interface of ultrasonically welded carbon fibre PPS joints. *Composites A* 2019;125:105574.
- [15] Tao W, Su X, Wang H, Zhang Z, Li H, Chen J. Influence mechanism of welding time and energy director to the thermoplastic composite joints by ultrasonic welding. *J Manuf Process* 2019;37:196–202.
- [16] Senders F, van Beurden M, Palardy G, Villegas IF. Zero-flow: A novel approach to continuous ultrasonic welding of CF/PPS thermoplastic composite plates. *Adv Manuf Polym Compos Sci* 2016;0340(September 2017):1–10.
- [17] Jongbloed Bram, Teuwen Julie, Palardy Genevieve, Villegas Irene Fernandez, Benedictus Rinze. Continuous ultrasonic welding of thermoplastic composites: Enhancing the weld uniformity by changing the energy director. *J Compos Mater* 2020;54(15):2023–35.
- [18] Rizzolo RH, Walczyk DF. Ultrasonic consolidation of thermoplastic composite prepreg for automated fiber placement. *J Thermoplast Compos Mater* 2015;1–18.
- [19] Chu Qiyi, Li Yong, Xiao Jun, Huan Dajun, Zhang Xiangyang, Chen Xiaodong. Processing and characterization of the thermoplastic composites manufactured by ultrasonic vibration-assisted automated fiber placement. *J Thermoplast Compos Mater* 2018;31(3):339–58.
- [20] Lionetto Francesca, Dell'Anna Riccardo, Montagna Francesco, Maffezzoli Alfonso. Modeling of continuous ultrasonic impregnation and consolidation of thermoplastic matrix composites. *Composites A* 2016;82:119–29.
- [21] Dell'Anna R, Lionetto F, Montagna F, Maffezzoli A. Lay-up and consolidation of a composite pipe by in situ ultrasonic welding of a thermoplastic matrix composite tape. *Materials* 2018;11(5). cited By 15.
- [22] Villegas IF, Palardy G. Ultrasonic welding of CF/PPS composites with integrated triangular energy directors: melting, flow and weld strength development. *Compos Interfaces* 2017;24(5):515–28.

- [23] Villegas Irene Fernandez. Ultrasonic welding of thermoplastic composites. *Front Mater* 2019;6:291.
- [24] Palardy Genevieve, Shi Huajie, Levy Arthur, Corre Steven Le, Villegas Irene Fernandez. A study on amplitude transmission in ultrasonic welding of thermoplastic composites. *Composites A* 2018;113:339–49.
- [25] Benatar A, Gutowski TG. Ultrasonic welding of PEEK graphite APC-2 composites. *Polym Eng Sci* 1989;29(23):1705–21.
- [26] TenCate. Product datasheet tencate cetex tc1100 PPS resin system, Nijverdal, The Netherlands. 2016, CETEX TC1100 V4 DS 090116.